Published by Nigerian Society of Physical Sciences. Hosted by FLAYOO Publishing House LTD

Proceedings of the Nigerian Society of Physical Sciences

Journal Homepage: https://flayoophl.com/journals/index.php/pnspsc

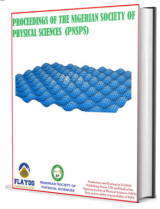

Unsteady dean flow of dusty fluids between two oscillating cylinders

Jibrin Danjuma Yahaya[a,*], Benedict Celestine Agbata[a], Rasaq Oyeyemi Olayiwola[a], Raji Muhammed[a], Isaac Adaji[a], Abdul Danjuma Yusuf[b], Emmanuel Olorunfemi Senewo[a]

[a]*Department of Mathematics and Statistics, Confluence University of Science and Technology, Osara, Kogi State, Nigeria*
[b]*Department of Actuarial Science, Confluence University of Science and Technology, Osara, Kogi State, Nigeria*

A B S T R A C T

This study investigates the unsteady Dean flow of dusty, viscous, incompressible fluids confined between two oscillating concentric horizontal cylinders under a semi-analytical framework based on Laplace transformation, which is preferred over fully numerical methods due to its ability to provide analytical expressions that enhance understanding of the system dynamics, reduce discretization errors, and efficiently handle complex boundary conditions. The Laplace-domain solutions are numerically inverted using the Riemann-sum approximation (RSA). The problem is modelled using the momentum and continuity equations for fluid and particulate phases, incorporating the effects of azimuthal pressure gradients and oscillatory boundary conditions. The semi-analytical framework is employed to derive the velocity profiles, skin frictions, and vorticity in the Laplace domain, which are then inverted to obtain time-dependent solutions. Steady-state solutions for the velocity, skin frictions, and vorticity (for the case of oscillation with different frequencies, non-oscillating cases, and oscillating with the same frequency) are obtained in closed forms to validate the method employed at large time values. Key dimensionless parameters such as the mass concentration of dust particles, relaxation time, dimensionless time, and angular velocities are explored to assess their impact on the flow dynamics. Results reveal that increasing relaxation time parameters delay the velocity profile and helps fluid velocity in achieving equilibrium flow states. The findings provide a benchmark for studies on industrial mixing, chemical reactors, and biomedical flows involving particle-laden fluids under oscillatory conditions.

Keywords: Unsteady-state, Dean flow, Riemann-sum approximation (RSA), Dust particles, Skin frictions, Dean vorticity.

DOI:10.61298/pnspsc.2025.2.157

1. INTRODUCTION

The study of fluid dynamics involving dusty fluids – fluids containing solid particles suspended within them – has garnered significant interest due to its relevance in both industrial applications and natural phenomena. One such intriguing problem is the unsteady Dean flow, which arises when a fluid flows between two rotating or oscillating cylinders, creating a complex secondary flow pattern due to the combined effects of centrifugal and Coriolis forces. In curved geometries, secondary flow structures (Dean vortices) emerge due to the imbalance between centrifugal forces and pressure gradients, causing fluid particles to move across streamlines and form counter-rotating vortices. The introduction of dust particles further complicates the flow

*Corresponding Author Tel. No.: +234-803-7662-510.
e-mail: yahayajd@custech.edu.ng (Jibrin Danjuma Yahaya)

dynamics, as the particles interact with the fluid, altering its velocity and pressure fields. This research aims to explore these intricate interactions by developing a semi-analytical approach to model the unsteady Dean flow of dusty fluids between two oscillating cylinders. The study provides valuable insights into the behaviour of such systems, which can be applied to enhance the design and efficiency of industrial processes such as chemical reactors, centrifuges, and sedimentation tanks.

Understanding the unsteady Dean flow of dusty fluids between oscillating cylinders has important applications across multiple fields. In combustion systems, plasma flows, industrial transport, and dust storm modelling, particle-fluid interactions are key to performance and safety. In the oil and gas industry, these insights support the design of efficient particle separation systems, improving operational efficiency and reducing costs. In biomedical engineering, the findings apply to blood flow and drug delivery systems, aiding the design of devices like artificial hearts and blood pumps. Additionally, in environmental engineering, they help optimize sediment management and sedimentation tank design. Overall, this study provides a practical framework for predicting and managing dusty fluid behaviour in complex engineering systems. The motion of a gas carrying small dust particles and its implications for various flow scenarios have been extensively studied, with significant contributions from numerous researchers.

Saffman [1] laid the foundation by formulating the equations for the motion of a gas with small dust particles and analyzing the stability of laminar flow. He found that fine dust destabilizes gas flow while coarse dust stabilizes it, modifying the Orr-Sommerfeld equation for a dusty gas. This work set the stage for understanding how dust concentration and relaxation time influence flow stability. Building on Saffman's work, Micheal and Norey [2] extended the analysis to the motion of a dusty gas between two impulsively rotating coaxial cylinders. They derived solutions for gas velocity and dust concentration, considering different time scales and boundary conditions, thus broadening the understanding of rotational flows in dusty gases. Miller [3] further explored the motion of dust particles around a vertically oscillating cylinder in an incompressible, viscous fluid. His explicit expressions for particle velocities and trajectories provided insights into particle behavior in oscillatory flows, highlighting the importance of particle size and oscillation parameters.

Reddy [4] investigated the laminar flow of an unsteady viscous liquid with uniformly distributed dust particles through an elliptic annulus. His analytical expressions for fluid and dust particle flow under various pressure gradients expanded the applicability of dusty gas flow models to different geometries. Gupta and Gupta [5] focused on the flow of a viscous incompressible gas with particles in circular and sectorial cylinders. Using operational calculus, they obtained exact velocities, providing numerical results for flow due to a constant pressure gradient and further enriching the theoretical framework for dusty gas flow in cylindrical geometries. Mitra and Bhattacharyya [6] examined the unsteady hydromagnetic laminar flow of an electrically conducting dusty fluid between two impulsively started parallel plates. Their work highlighted the influence of dust concentration, relaxation time, and Hartmann number on velocity fields, showing how magnetic fields can modulate dusty fluid flow. Rukmangadachari and Arunachalam [7] studied the unsteady laminar flow of a dusty fluid through a triangular cross-section cylinder, examining harmonic and exponential pressure gradients. They calculated velocity fields, flux, and skin friction drag, contributing valuable data for flows in non-circular cross-sections. Debnath and Ghosh [8] explored the motion of an incompressible viscous conducting fluid with small spherical particles between two oscillating plates in a transverse magnetic field. Their exact solutions using operational methods elucidated the impact of oscillation time periods on fluid velocity, further integrating magnetic effects into dusty fluid dynamics. Hamdan and Barron [9] introduced a dusty fluid flow model in porous media, solving numerically for flow in a rectangular cavity. Their comparisons with clean fluid flow results underscored the differences caused by dust particles in porous media, expanding the scope of dusty fluid flow studies. Vajravelu and Nayfeh [10] analyzed the hydromagnetic flow of a dusty fluid over a stretching sheet, reducing the motion equations to coupled non-linear ordinary differential equations and solving them numerically. They discussed fluid-particle interaction, particle loading, and suction effects, thereby addressing practical applications in stretching sheet scenarios. Hamdan and Barron [11] extended their previous work by developing partial differential equations for dusty fluid flow in porous media using volume-averaging techniques. They considered one-way and two-way interactions between phases, providing a comprehensive framework for analyzing dusty fluid flow in porous structures.

Yang, Eidelman, and Lottati [12] studied unsteady shock-wave reflection and diffraction over a semicircular cylinder in a dusty gas using a multifluid Eulerian approach. Their model validation with experimental data offered insights into the effects of particle size and loading on shock-wave configurations, bridging the gap between theoretical models and experimental observations. Datta and Dalal [13] investigated pulsatile flow and heat transfer of a dusty fluid in an annulus of circular cylinders under pulsatile pressure gradients. Using Saffman's model, they provided analytical solutions, discussing velocity and heat transfer variations with annular gap and oscillation frequency, thereby integrating pulsatile flow dynamics into dusty fluid studies. Atria [14] examined the effect of variable viscosity on the transient flow of a dusty fluid with heat transfer under a constant pressure gradient and a transverse magnetic field. Numerical solutions revealed the impact of viscosity and magnetic field on flow and heat transfer, emphasizing the role of variable properties in dusty fluid dynamics. Allan *et al.* [15] developed partial differential equations for dusty fluid flow in variable porosity media, solving them numerically for different porous media parameters. Their analysis provided valuable insights into the effects of porous media characteristics on dusty fluid flow.

Volkov and Tsirkunov [16] modeled supersonic dusty-gas flow around a cylinder, accounting for particle-particle collisions and feedback effects on gas parameters. They identified parameter ranges where collisions and feedback are significant, contributing to the understanding of high-speed dusty gas flows. [17, 18] conducted analytical studies on unsteady viscous dusty fluid flow between parallel plates and through rectangular channels under pulsatile pressure gradients. Using Laplace transform techniques, they discussed velocity profiles and skin friction, thereby

enhancing the theoretical models for unsteady dusty fluid flows. Makinde and Chinyoka [19] explored the unsteady flow and heat transfer of a dusty fluid between parallel plates with variable viscosity and electric conductivity under a magnetic field. Using a semi-implicit finite difference scheme, they discussed the effects of wall slip, viscosity, and electric conductivity variations, thus addressing complex interactions in dusty fluid flows.

Eguía *et al.* [20] investigated MHD Couette flow of a dusty conducting fluid with variable viscosity and electric conductivity. They used the network simulation method (NSM) and Pspice to solve the flow and heat transfer problems, analyzing the effects of viscosity, magnetic field, particle concentration, and upper wall velocity, thereby integrating modern computational techniques into dusty fluid dynamics. This extensive body of work collectively advances the understanding of dusty fluid dynamics, addressing various flow configurations, geometries, and influencing factors. The integration of magnetic fields, variable properties, and computational methods further enriches the theoretical and practical knowledge in this domain.

2. PROBLEM STATEMENT AND MATHEMATICAL ANALYSIS

In this work, we consider the unsteady-state Dean flow of a viscous, incompressible non-Newtonian dusty fluid in the annular space between two infinite concentric oscillating cylinders under a constant azimuthal pressure gradient. The inner and outer radii of the cylinders are r_1 and r_2, respectively. Initially, at $t^* < 0$, the fluid and dust particles are at rest, and the flow is initiated by the azimuthal pressure gradient and the oscillation of the boundary. The flow occurs only in the annular region $r_2 - r_1$ (with $r_2 > r_1$), and all physical variables, except for pressure, depend only on the dimensionless radial coordinate r^* and time t^*. The channel is infinitely long, and the flow is assumed to be fully developed, with the radial velocity component to be zero i.e $v_r = 0$, and the continuity equation depends solely on r^* and t^*. The dynamics of the dusty fluid and particles are described by the modified Saffman's equation [1, 21]:

$$\varrho\frac{u_r^*}{r^*} = \frac{\partial p}{\partial r^*}, \tag{1}$$

$$\varrho\frac{\partial u^*}{\partial t^*} = -\frac{1}{r^*}\frac{\partial p}{\partial \varphi}+\mu\left(\frac{\partial^2 u^*}{\partial r^{*2}} + \frac{1}{r^*}\frac{\partial u^*}{\partial r^*} - \frac{u^*}{r^{*2}}\right)+KN\,(v^* - u^*)\,, \tag{2}$$

$$m\frac{\partial v^*}{\partial t^*} = K\,(u^* - v^*)\,, \tag{3}$$

with the initial and boundary conditions:

$$\begin{aligned} &t \le 0 : u^* = v^* = 0 \; for \; r_1 \le r^* \le r_2 \\ &t > 0 \begin{cases} u^* = a^* e^{i\omega_1 t^*} + b^* e^{-i\omega_1 t^*} \; at \; r^* = r_1 \\ u^* = c^* e^{i\omega_2 t^*} + d^* e^{-i\omega_2 t^*} \; at \; r^* = r_2, \end{cases} \end{aligned} \tag{4}$$

where u^* and v^* are the velocities of the fluid and dust particle respectively, ρ the density of the fluid, p is the pressure along the azimuthal direction, t^* the time, μ is the viscosity coefficient of the fluid, K is the Stoke's resistance coefficient $6\pi\mu a$ of spherical particles of radius a, N is the density of the dust particles, m mass of the dust particles, r_1 and r_2 are the radius of the inner and outer cylinders, and ω_1 and ω_2 the oscillatory frequency of the inner and outer cylinders respectively. The flow geometry is depicted as shown in Fig. 1. The azimuthal pressure gradient drives the primary circumferential flow and, combined with curvature effects, induces secondary Dean vortices within the annular gap.

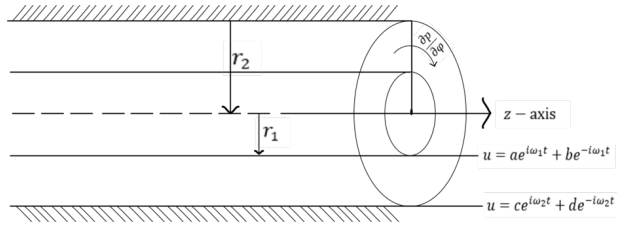

Figure 1. Configuration of the flow geometry.

3. DIMENSIONAL ANALYSIS

Using the following dimensionless quantities [21, 22]:

$$\begin{aligned} &r = \frac{r^*}{r_1},\; \lambda = \frac{r_2}{r_1}, t = \frac{\upsilon t^*}{r_1^2},\; u = \frac{u^*}{U_0},\; v = \frac{v^*}{U_0},\; \tau = \frac{\upsilon m}{r_1^2 K}, \\ &\iota = \frac{mN}{\varrho},\; U_0 = -\frac{r_1^2}{\upsilon^2\varrho}\frac{\partial p}{\partial \varphi},\; \sigma_1 = \frac{r_1^2}{\upsilon}\omega_1,\; \sigma_2 = \frac{r_1^2}{\upsilon}\omega_2, \\ &a = \frac{a^*}{U_0}, b = \frac{b^*}{U_0}, c = \frac{c^*}{U_0},\; d = \frac{d^*}{U_0}, \end{aligned} \tag{5}$$

Equations (2) to (4) reduce to:

$$\frac{\partial u}{\partial t} = \frac{1}{r} + \left(\frac{\partial^2 u}{\partial r^2} + \frac{1}{r}\frac{\partial u}{\partial r} - \frac{u}{r^2}\right) + \frac{l}{\tau}\,(v - u)\,, \tag{6}$$

$$\frac{\partial v}{\partial t} = \frac{1}{\tau}\,(u - v)\,, \tag{7}$$

$$\begin{aligned} &t \le 0 : u = v = 0 \; for \; 1 \le r \le \lambda \\ &t > 0 \begin{cases} u = ae^{i\sigma_1 t} + be^{-i\sigma_1 t} \; at \; r = 1 \\ u = ce^{i\sigma_2 t} + de^{-i\sigma_2 t} \; at \; r = \lambda \end{cases}, \end{aligned} \tag{8}$$

where a, b, c, and d are complex constants such that u becomes real on the boundary.

4. METHODOLOGY

4.1. UNSTEADY-STATE SOLUTIONS

4.1.1. Velocity profile

The solution of Equations (6) and (7) under the boundary conditions of Equation (8) is sought using the Laplace transform technique. Applying Laplace transform technique [23, 24]:

$$\mathcal{L}\,(u\,(r,t)) = \bar{u}\,(r,\varsigma) = \int_0^\infty u\,(r,t)\,e^{-\varsigma t}dt,\; \varsigma > 0, \tag{9}$$

$$\mathcal{L}\,(v\,(r,t)) = \bar{v}\,(r,\varsigma) = \int_0^\infty v\,(r,t)\,e^{-\varsigma t}dt,\; \varsigma > 0, \tag{10}$$

Equations (6) to (8) yield

$$\frac{d^2\bar{u}}{dr^2} + \frac{1}{r}\frac{d\bar{u}}{dr} - \frac{1}{r^2}\left[1 + \left(\frac{l\varsigma}{1+\tau\varsigma} + \varsigma\right)r^2\right]\bar{u} = -\frac{1}{r\varsigma}, \tag{11}$$

$$\bar{v} = \frac{\bar{u}}{1+\tau\varsigma}, \tag{12}$$

$$\begin{aligned}\bar{u} &= \tfrac{a}{\varsigma-i\sigma_1} + \tfrac{b}{\varsigma+i\sigma_1} \; at \; r = 1\\ \bar{u} &= \tfrac{c}{\varsigma-i\sigma_2} + \tfrac{d}{\varsigma+i\sigma_2} \; at \; r = \lambda,\end{aligned} \tag{13}$$

where ι is the mass concentration of the dust particles, τ is the relaxation time parameter, σ_1 and σ_2 are oscillatory parameters and ς is the Laplace parameter.

Using the transformation [25]:

$$\bar{u}(r,\varsigma) = \bar{u}_h(r,\varsigma) + \frac{1}{r\varsigma A^2} \tag{14}$$

on Equation (11), then, the general solution, under the boundary conditions of Equation (13) is given as:

$$\bar{u}(r,\varsigma) = D_1 I_1(rA) + D_2 K_1(rA) + \frac{1}{r\varsigma A^2}, \tag{15}$$

$$A^2 = \left[\varsigma + \frac{l\varsigma}{1+\tau\varsigma}\right], \tag{16}$$

Then, from Equation (12), the velocity of the dust particles is given as:

$$\begin{aligned}\bar{v}(r,\varsigma) &= \frac{\bar{u}}{1+\tau\varsigma}\\ &= \frac{1}{1+\tau\varsigma}\left[D_1 I_1(rA) + D_2 K_1(rA) + \frac{1}{r\varsigma A^2}\right].\end{aligned} \tag{17}$$

Case I: $a \neq b \neq c \neq d \neq 0$
Equations (15) and (17) are the velocity of the fluid and dust particles in the Laplace domain. D_1 and D_2 are constants obtained by applying the boundary conditions Equation (13), we have:

$$\begin{aligned}D_1 = &\frac{a}{(\varsigma - i\sigma_1) I_1(A)} + \frac{b}{(\varsigma + i\sigma_1) I_1(A)}\\ &- D_2\frac{K_1(A)}{I_1(A)} - \frac{1}{\varsigma A^2 I_1(A)},\end{aligned} \tag{18}$$

$$D_2 = \frac{a_1 - a_2 + a_3}{a_4}, \tag{19}$$

where

$$\begin{aligned}a_1 &= \lambda\varsigma^2 A^4\left(\varsigma^2 + {\sigma_2}^2\right) I_1(A\lambda)\left((a+b)\varsigma + i\sigma_1(a-b)\right)\\ a_2 &= \lambda\varsigma^2 A^4\left(\varsigma^2 + {\sigma_1}^2\right) I_1(A)\left((c+d)\varsigma + i\sigma_2(c-d)\right)\\ a_3 &= \varsigma A^2\left(\varsigma^2 + {\sigma_1}^2\right)\left(\varsigma^2 + {\sigma_2}^2\right)\left(I_1(A) - \lambda I_1(A\lambda)\right)\\ a_4 &= \lambda\varsigma^2 A^4\left(\varsigma^2 + {\sigma_1}^2\right)\left(\varsigma^2 + {\sigma_2}^2\right)\left(K_1(A) I_1(A\lambda) - K_1(A\lambda) I_1(A)\right).\end{aligned}$$

Case II: $a = b = c = d = 0$ (Static boundary)
For the special case of no impulsive motion at the boundary, the velocity of the fluid and dust particles are given in Equations (20) and (21) as follows:

$$\bar{u}(r,\varsigma) = D_3 I_1(rA) + D_4 K_1(rA) + \frac{1}{r\varsigma A^2}, \tag{20}$$

$$\begin{aligned}\bar{v}(r,\varsigma) &= \frac{\bar{u}}{1+\tau\varsigma}\\ &= \frac{1}{1+\tau\varsigma}\left[D_3 I_1(rA) + D_4 K_1(rA) + \frac{1}{r\varsigma A^2}\right],\end{aligned} \tag{21}$$

where

$$D_3 = -D_4\frac{K_1(A)}{I_1(A)} - \frac{1}{\varsigma A^2 I_1(A)}, \tag{22}$$

$$D_4 = \frac{I_1(A) - \lambda I_1(A\lambda)}{\lambda\varsigma A^2\left(K_1(A) I_1(A\lambda) - K_1(A\lambda) I_1(A)\right)}. \tag{23}$$

Case III: $\sigma_1 = \sigma_2 = 0$ (non-oscillating case)
For the case of non-oscillatory motion at the boundary, the velocity of the fluid and dust particles are given in Equations (24) and (25) in similar manners as follows:

$$\bar{u}(r,\varsigma) = D_5 I_1(rA) + D_6 K_1(rA) + \frac{1}{r\varsigma A^2}, \tag{24}$$

$$\begin{aligned}\bar{v}(r,\varsigma) &= \frac{\bar{u}}{1+\tau\varsigma}\\ &= \frac{1}{1+\tau\varsigma}\left[D_5 I_1(rA) + D_6 K_1(rA) + \frac{1}{r\varsigma A^2}\right],\end{aligned} \tag{25}$$

$$D_5 = \frac{a+b}{\varsigma I_1(A)} - D_6\frac{K_1(A)}{I_1(A)} - \frac{1}{\varsigma A^2 I_1(A)}, \tag{26}$$

$$D_6 = \frac{a_5 + a_6}{a_7}, \tag{27}$$

where

$$\begin{aligned}a_5 &= \lambda\varsigma^5 A^4\left(I_1(A\lambda)(a+b) - I_1(A)(c+d)\right)\\ a_6 &= \varsigma^5 A^2\left(I_1(A) - \lambda I_1(A\lambda)\right)\\ a_7 &= \lambda\varsigma^6 A^4\left(K_1(A) I_1(A\lambda) - K_1(A\lambda) I_1(A)\right).\end{aligned} \tag{28}$$

Case IV: $\sigma_1 = \sigma_2 = \sigma$ (Oscillating with the same frequency)
For the case of oscillatory motion with equal frequency at the boundary, the velocity of the fluid and dust particles are given in Equations (29) and (30) in similar manners as follows:

$$\bar{u}(r,\varsigma) = D_7 I_1(rA) + D_8 K_1(rA) + \frac{1}{r\varsigma A^2}, \tag{29}$$

$$\begin{aligned}\bar{v}(r,\varsigma) &= \frac{\bar{u}}{1+\tau\varsigma}\\ &= \frac{1}{1+\tau\varsigma}\left[D_7 I_1(rA) + D_8 K_1(rA) + \frac{1}{r\varsigma A^2}\right],\end{aligned} \tag{30}$$

$$D_7 = \frac{(a+b)\varsigma - i(a-b)\sigma}{(\varsigma^2+\sigma^2) I_1(A)} - D_8\frac{K_1(A)}{I_1(A)} - \frac{1}{\varsigma A^2 I_1(A)}, \tag{31}$$

$$D_8 = \frac{a_8 - a_9 + a_{10}}{a_{11}}, \tag{32}$$

where

$$\begin{aligned}a_8 &= \lambda\varsigma^2 A^4\left(\varsigma^2 + \sigma^2\right) I_1(A\lambda)\left((a+b)\varsigma + i(a-b)\sigma\right)\\ a_9 &= \lambda\varsigma^2 A^4\left(\varsigma^2 + \sigma^2\right) I_1(A)\left((c+d)\varsigma + i(c-d)\sigma\right)\\ a_{10} &= \varsigma A^2\left(\varsigma^2 + \sigma^2\right)^2\left(I_1(A) - \lambda I_1(A\lambda)\right)\\ a_{11} &= \lambda\varsigma^2 A^4\left(\varsigma^2 + \sigma^2\right)^2\left(K_1(A) I_1(A\lambda) - K_1(A\lambda) I_1(A)\right).\end{aligned}$$

4.1.2. Skin frictions

The skin frictions between the fluid layers and of the dust particles in a concentric cylinder are given as follows:

$$\bar{\chi}|_r = \left(\frac{d\bar{u}}{dr} - \frac{\bar{u}}{r}\right)\bigg|_r, \tag{33a}$$

$$\bar{\chi}|_{rp} = \frac{1}{1+\tau\varsigma}\left(\frac{d\bar{u}}{dr} - \frac{\bar{u}}{r}\right)\bigg|_r. \tag{33b}$$

Case I: $a \neq b \neq c \neq d \neq 0$

The skin frictions for the fluids and dust particles are obtained as follows:

$$\bar{\chi}_1 = \left(\frac{d\bar{u}}{dr} - \frac{\bar{u}}{r}\right)\bigg|_{r=1} = A\left[D_{\,1}I_2(A) - D_2K_2(A)\right] - \frac{2}{\varsigma A^2}, \tag{34a}$$

$$\begin{aligned}\bar{\chi}_\lambda &= \left(\frac{d\bar{u}}{dr} - \frac{\bar{u}}{r}\right)\bigg|_{r=\lambda} \\ &= A\left[D_1I_2(A\lambda) - D_2K_2(A\lambda)\right] - \frac{2}{\lambda^2\varsigma A^2},\end{aligned} \tag{34b}$$

$$\begin{aligned}\bar{\chi}_{1p} &= \frac{1}{1+\tau\varsigma}\left(\frac{d\bar{u}}{dr} - \frac{\bar{u}}{r}\right)\bigg|_{r=1} \\ &= \frac{1}{1+\tau\varsigma}\left[A\left(D_1I_2(A) - D_2K_2(A)\right)\right] - \frac{2}{(1+\tau\varsigma)\,\varsigma A^2},\end{aligned} \tag{35a}$$

$$\begin{aligned}\bar{\chi}_{\lambda p} &= \frac{1}{1+\tau\varsigma}\left(\frac{d\bar{u}}{dr} - \frac{\bar{u}}{r}\right)\bigg|_{r=\lambda} \\ &= \frac{1}{1+\tau\varsigma}\left[A\left(D_1I_2(A) - D_2K_2(A)\right)\right] \\ &\quad - \frac{2}{(1+\tau\varsigma)\,\lambda^2\varsigma A^2}.\end{aligned} \tag{35b}$$

Case II: $a = b = c = d = 0$

$$\bar{\chi}_1 = \left(\frac{d\bar{u}}{dr} - \frac{\bar{u}}{r}\right)\bigg|_{r=1} = A\left[D_3I_2(A) - D_4K_2(A)\right] - \frac{2}{\varsigma A^2}, \tag{36a}$$

$$\begin{aligned}\bar{\chi}_\lambda &= \left(\frac{d\bar{u}}{dr} - \frac{\bar{u}}{r}\right)\bigg|_{r=\lambda} \\ &= A\left[D_3I_2(A\lambda) - D_4K_2(A\lambda)\right] - \frac{2}{\lambda^2\varsigma A^2},\end{aligned} \tag{36b}$$

$$\begin{aligned}\bar{\chi}_{1p} &= \frac{1}{1+\tau\varsigma}\left(\frac{d\bar{u}}{dr} - \frac{\bar{u}}{r}\right)\bigg|_{r=1} \\ &= \frac{1}{1+\tau\varsigma}\left[A\left(D_1I_2(A) - D_2K_2(A)\right)\right] - \frac{2}{(1+\tau\varsigma)\,\varsigma A^2},\end{aligned} \tag{37a}$$

$$\begin{aligned}\bar{\chi}_{\lambda p} &= \frac{1}{1+\tau\varsigma}\left(\frac{d\bar{u}}{dr} - \frac{\bar{u}}{r}\right)\bigg|_{r=\lambda} \\ &= \frac{1}{1+\tau\varsigma}\left[A\left(D_1I_2(A) - D_2K_2(A)\right)\right] \\ &\quad - \frac{2}{(1+\tau\varsigma)\,\lambda^2\varsigma A^2}.\end{aligned} \tag{37b}$$

Case III: $\sigma_1 = \sigma_2 = 0$ (non-oscillating case)

$$\bar{\chi}_1 = \left(\frac{d\bar{u}}{dr} - \frac{\bar{u}}{r}\right)\bigg|_{r=1} = A\left[D_5I_2(A) - D_6K_2(A)\right] - \frac{2}{\varsigma A^2}, \tag{38a}$$

$$\begin{aligned}\bar{\chi}_\lambda &= \left(\frac{d\bar{u}}{dr} - \frac{\bar{u}}{r}\right)\bigg|_{r=\lambda} \\ &= A\left[D_5I_2(A\lambda) - D_6K_2(A\lambda)\right] - \frac{2}{\lambda^2\varsigma A^2},\end{aligned} \tag{38b}$$

$$\begin{aligned}\bar{\chi}_{1p} &= \frac{1}{1+\tau\varsigma}\left(\frac{d\bar{u}}{dr} - \frac{\bar{u}}{r}\right)\bigg|_{r=1} \\ &= \frac{1}{1+\tau\varsigma}\left[A\left(D_1I_2(A) - D_2K_2(A)\right)\right] - \frac{2}{(1+\tau\varsigma)\,\varsigma A^2},\end{aligned} \tag{39a}$$

$$\begin{aligned}\bar{\chi}_{\lambda p} &= \frac{1}{1+\tau\varsigma}\left(\frac{d\bar{u}}{dr} - \frac{\bar{u}}{r}\right)\bigg|_{r=\lambda} \\ &= \frac{1}{1+\tau\varsigma}\left[A\left(D_1I_2(A) - D_2K_2(A)\right)\right] \\ &\quad - \frac{2}{(1+\tau\varsigma)\,\lambda^2\varsigma A^2}.\end{aligned} \tag{39b}$$

Case IV: $\sigma_1 = \sigma_2 = \sigma$ (Oscillating with the same frequency)

$$\bar{\chi}_1 = \left(\frac{d\bar{u}}{dr} - \frac{\bar{u}}{r}\right)\bigg|_{r=1} = A\left[D_7I_2(A) - D_8K_2(A)\right] - \frac{2}{\varsigma A^2}, \tag{40a}$$

$$\begin{aligned}\bar{\chi}_\lambda &= \left(\frac{d\bar{u}}{dr} - \frac{\bar{u}}{r}\right)\bigg|_{r=\lambda} \\ &= A\left[D_7I_2(A\lambda) - D_8K_2(A\lambda)\right] - \frac{2}{\lambda^2\varsigma A^2},\end{aligned} \tag{40b}$$

$$\begin{aligned}\bar{\chi}_{1p} &= \frac{1}{1+\tau\varsigma}\left(\frac{d\bar{u}}{dr} - \frac{\bar{u}}{r}\right)\bigg|_{r=1} \\ &= \frac{1}{1+\tau\varsigma}\left[A\left(D_1I_2(A) - D_2K_2(A)\right)\right] - \frac{2}{(1+\tau\varsigma)\,\varsigma A^2},\end{aligned} \tag{41a}$$

$$\begin{aligned}\bar{\chi}_{\lambda p} &= \frac{1}{1+\tau\varsigma}\left(\frac{d\bar{u}}{dr} - \frac{\bar{u}}{r}\right)\bigg|_{r=\lambda} \\ &= \frac{1}{1+\tau\varsigma}\left[A\left(D_1I_2(A) - D_2K_2(A)\right)\right] \\ &\quad - \frac{2}{(1+\tau\varsigma)\,\lambda^2\varsigma A^2}.\end{aligned} \tag{41b}$$

4.1.3. Vorticity

The vorticity of the fluid flow is defined as the swirling motion of the fluid. Since the fluid flow is in the azimuthal direction, then the vorticity is the z-direction. The formulae are given as:

$$\bar{w}_z = \left(\frac{d\bar{u}}{dr} + \frac{\bar{u}}{r}\right), \tag{42a}$$

and also, the vorticity of the dust particle is given by:

$$\bar{w}_{zp} = \frac{1}{1+\tau\varsigma}\left(\frac{d\bar{u}}{dr} + \frac{\bar{u}}{r}\right). \tag{42b}$$

Case I: $a \neq b \neq c \neq d \neq 0$

Using the formulae of Equations (42a) and (42b), the vorticity of the fluid and of the dust particle are given by:

$$\bar{w}_z = A\left[D_1I_0(rA) - D_2K_0(rA)\right], \tag{43a}$$

$$\bar{w}_{zp} = \frac{1}{1+\tau\varsigma}\left(A\left(D_1I_0(rA) - D_2K_0(rA)\right)\right). \tag{43b}$$

Case II: $a = b = c = d = 0$

$$\bar{w}_z = A\left[D_3 I_0(rA) - D_4 K_0(rA)\right], \tag{44a}$$

$$\bar{w}_{zp} = \frac{1}{1+\tau\varsigma}\left(A\left(D_3 I_0(rA) - D_4 K_0(rA)\right)\right). \tag{44b}$$

Case III: $\sigma_1 = \sigma_2 = 0$ (non-oscillating case)

$$\bar{w}_z = A\left[D_5 I_0(rA) - D_6 K_0(rA)\right], \tag{45a}$$

$$\bar{w}_{zp} = \frac{1}{1+\tau\varsigma}\left(A\left(D_5 I_0(rA) - D_6 K_0(rA)\right)\right), \tag{45b}$$

Case IV: $\sigma_1 = \sigma_2 = \sigma$ (Oscillating with the same frequency)

$$\bar{w}_z = A\left[D_7 I_0(rA) - D_8 K_0(rA)\right], \tag{46a}$$

$$\bar{w}_{zp} = \frac{1}{1+\tau\varsigma}\left(A\left(D_7 I_0(rA) - D_8 K_0(rA)\right)\right). \tag{46b}$$

4.2. STEADY-STATE SOLUTIONS

The steady-state solutions are provided to validate the semi-analytical Laplace domain solutions, as transient results are expected to converge to steady behaviour at large times. Closed-form expressions for velocity, skin friction, and vorticity under steady conditions (including non-oscillating and various oscillating cases) confirm the physical consistency and reliability of the transient solutions and their numerical inversion.

4.2.1. Steady-state velocity profile

For steady-state solutions, $\frac{\partial u}{\partial t} = 0$ and $\frac{\partial v}{\partial t} = 0$ in Equations (6) and (7), respectively, we have that:

$$u_s = v_s, \tag{33}$$

$$\frac{d^2u}{dr^2} + \frac{1}{r}\frac{du}{dr} - \frac{u}{r^2} = -\frac{1}{r}. \tag{34}$$

Case I: $a \neq b \neq c \neq d \neq 0$

Eq (34) is a non-homogeneous ordinary differential equation called the Euler equation whose solution is given as:

$$u_s(r) = D_9 r + \frac{D_{10}}{r} - \frac{r}{2}\ln(r), \tag{35}$$

D_9 and D_{10} are constants obtained using the boundary conditions of (8) and they are:

$$D_9 = \frac{2\left\{\left[ae^{i\sigma_1 t} + be^{-i\sigma_1 t}\right] - \lambda\left[ce^{i\sigma_2 t} + de^{-i\sigma_2 t}\right]\right\} - \lambda^2\ln(\lambda)}{2(1-\lambda^2)},$$

$$D_{10} = \frac{2\left\{\lambda^2\left[ae^{i\sigma_1 t} + be^{-i\sigma_1 t}\right] - \lambda\left[ce^{i\sigma_2 t} + de^{-i\sigma_2 t}\right]\right\} - \lambda^2\ln(\lambda)}{2(\lambda^2-1)}.$$

Case II: $a = b = c = d = 0$

For the case of no impulsive motion at the boundary, the steady-state velocity is given as:

$$u_s(r) = \frac{\lambda^2 r\ln(\lambda)}{(\lambda^2-1)} - \frac{\lambda^2\ln(\lambda)}{(\lambda^2-1)r} - \frac{r}{2}\ln(r). \tag{36}$$

For $a = b = c = d = 0$, the steady-state velocity of Eq (36) is the velocity profile for transient Dean flow in an annulus as obtained in the work of Ref. [22].

Case III: $\sigma_1 = \sigma_2 = 0$ (non-oscillating case)

For non-oscillation at the boundary, the steady-state velocity is obtained similarly as:

$$u_s(r) = D_{11} r + \frac{D_{12}}{r} - \frac{r}{2}\ln(r). \tag{37}$$

D_{11} and D_{12} are obtained as:

$$D_{11} = \frac{2\left\{(a+b) - \lambda(c+d) - \lambda^2\ln(\lambda)\right\}}{2(1-\lambda^2)},$$

$$D_{12} = \frac{2\left\{\lambda^2(a+b) - \lambda(c+d) - \lambda^2\ln(\lambda)\right\}}{2(\lambda^2-1)}.$$

Case IV: $\sigma_1 = \sigma_2 = \sigma$ (Oscillating with the same frequency)

The steady-state velocity for when the frequency of oscillation are equal is obtained as:

$$u_s(r) = D_{13} r + \frac{D_{14}}{r} - \frac{r}{2}\ln(r). \tag{38}$$

$$D_{13} = \frac{2\left[(a-\lambda c)e^{i\sigma t} + (b-\lambda d)e^{-i\sigma t} - \lambda^2\ln(\lambda)\right]}{2(1-\lambda^2)},$$

$$D_{14} = \frac{2\left\{\lambda\left[(a\lambda - c)e^{i\sigma t} + (b\lambda - d)e^{-i\sigma t}\right] - \lambda^2\ln(\lambda)\right\}}{2(\lambda^2-1)}.$$

4.2.2. Steady-state skin frictions

Using the same approach for the unsteady-state skin frictions, the following skin frictions are derived for the different cases.

Case I: $a \neq b \neq c \neq d \neq 0$

The steady-state skin frictions at $r = 1$ and $r = \lambda$ for case I is:

$$\chi_{s1} = r\frac{d}{dr}\left(\frac{u_s}{r}\right)\Big|_{r=1} = -2D_{10} - \frac{1}{2}, \tag{39}$$

$$\chi_{s\lambda} = r\frac{d}{dr}\left(\frac{u_s}{r}\right)\Big|_{r=\lambda} = -\frac{2D_{10}}{\lambda^2} - \frac{1}{2}. \tag{40}$$

Case II: $a = b = c = d = 0$

$$\chi_{s1} = r\frac{d}{dr}\left(\frac{u_s}{r}\right)\Big|_{r=1} = -2D_{10} - \frac{1}{2}, \tag{41}$$

$$\chi_{s\lambda} = r\frac{d}{dr}\left(\frac{u_s}{r}\right)\Big|_{r=\lambda} = -\frac{2D_{10}}{\lambda^2} - \frac{1}{2}. \tag{42}$$

Case III: $\sigma_1 = \sigma_2 = 0$ (non-oscillating case)

$$\chi_{s1} = r\frac{d}{dr}\left(\frac{u_s}{r}\right)\Big|_{r=1} = -2D_{12} - \frac{1}{2}, \tag{43}$$

$$\chi_{s\lambda} = r\frac{d}{dr}\left(\frac{u_s}{r}\right)\Big|_{r=\lambda} = -\frac{2D_{12}}{\lambda^2} - \frac{1}{2}. \tag{44}$$

Case IV: $\sigma_1 = \sigma_2 = \sigma$ (Oscillating with the same frequency)

$$\chi_{s1} = r\frac{d}{dr}\left(\frac{u_s}{r}\right)\Big|_{r=1} = -2D_{12} - \frac{1}{2}, \tag{45}$$

$$\chi_{s\lambda} = r\frac{d}{dr}\left(\frac{u_s}{r}\right)\Big|_{r=\lambda} = -\frac{2D_{12}}{\lambda^2} - \frac{1}{2}. \tag{46}$$

4.2.3. Steady-state vorticity

The steady-state vorticity, in a similar manner, are obtained as follows.

Case I: $a \neq b \neq c \neq d \neq 0$

On utilizing Eq (35), the steady-state vorticity of the fluid is calculated thus:

$$w_{zs} = \frac{1}{r}\frac{d}{dr}(ru_s) = 2D_9 - \left(\ln(r) + \frac{1}{2}\right). \tag{47}$$

Case II: $a = b = c = d = 0$

$$w_{zs} = \frac{1}{r}\frac{d}{dr}(ru_s) = \frac{1 - \lambda^2 - \lambda^2 \ln(\lambda)}{2(\lambda^2 - 1)} - \ln(r). \tag{48}$$

Case III: $\sigma_1 = \sigma_2 = 0$ (non-oscillating case)

$$w_{zs} = \frac{1}{r}\frac{d}{dr}(ru_s) = 2D_{11} - \left(\ln(r) + \frac{1}{2}\right). \tag{49}$$

Case IV: $\sigma_1 = \sigma_2 = \sigma$ (Oscillating with the same frequency)

$$w_{zs} = \frac{1}{r}\frac{d}{dr}(ru_s) = 2D_{13} - \left(\ln(r) + \frac{1}{2}\right). \tag{50}$$

5. RIEMANN-SUM APPROXIMATIONS

The analytical Laplace inversion of Equations (15), (17), (20), (21), (24), (25), (29), (30), (34a - 41b), and (43a – 46b) are challenging due to their complexity. However, the RSA method (Equations 51 – 55), as employed in refs. [26–28], efficiently transforms solutions from the Laplace domain to the time domain.

$$\mathcal{L}^{-1}[\bar{u}(r,\varsigma)] = u(r,t) = \frac{e^{\epsilon t}}{t}\left[\frac{1}{2}\bar{u}(r,\epsilon) + Re\sum_{k=1}^{n}\bar{u}\left(r,\epsilon + \frac{ik\pi}{t}\right)(-1)^k\right], \tag{51}$$

$$\mathcal{L}^{-1}[\bar{v}(r,\varsigma)] = v(r,t) = \frac{e^{\epsilon t}}{t}\left[\frac{1}{2}\bar{v}(r,\epsilon) + Re\sum_{k=1}^{n}\bar{v}\left(r,\epsilon + \frac{ik\pi}{t}\right)(-1)^k\right], \tag{52}$$

$$\mathcal{L}^{-1}[\bar{\chi}_1(r,\varsigma)] = \chi_1(r,t) = \frac{e^{\epsilon t}}{t}\left[\frac{1}{2}\bar{\chi}_1(r,\epsilon) + Re\sum_{k=1}^{n}\bar{\chi}_1\left(r,\epsilon + \frac{ik\pi}{t}\right)(-1)^k\right], \tag{53}$$

$$\mathcal{L}^{-1}[\bar{\chi}_\lambda(r,\varsigma)] = \chi_\lambda(r,t) = \frac{e^{\epsilon t}}{t}\left[\frac{1}{2}\bar{\chi}_\lambda(r,\epsilon) + Re\sum_{k=1}^{n}\bar{\chi}_\lambda\left(r,\epsilon + \frac{ik\pi}{t}\right)(-1)^k\right], \tag{54}$$

$$\mathcal{L}^{-1}[\bar{w}_z(r,\varsigma)] = w_z(r,t) = \frac{e^{\epsilon t}}{t}\left[\frac{1}{2}\bar{w}_z(r,\epsilon) + Re\sum_{k=1}^{n}\bar{w}_z\left(r,\epsilon + \frac{ik\pi}{t}\right)(-1)^k\right]. \tag{55}$$

In this numerical approach, functions in the ς-domain are converted to the time domain. The term Re denotes the real part, $i = \sqrt{-1}$ is the imaginary unit, n represents the number of terms in the RSA (here $n = 1000$), and ϵ is the real part of the Bromwich contour used for Laplace transform inversion. As per Ref. [29], ϵ must enclose all branch points, with $\epsilon t = 4.7$ yielding optimal results and faster convergence. The RSA method is validated by computing steady-state velocity, shear stress, and vorticity.

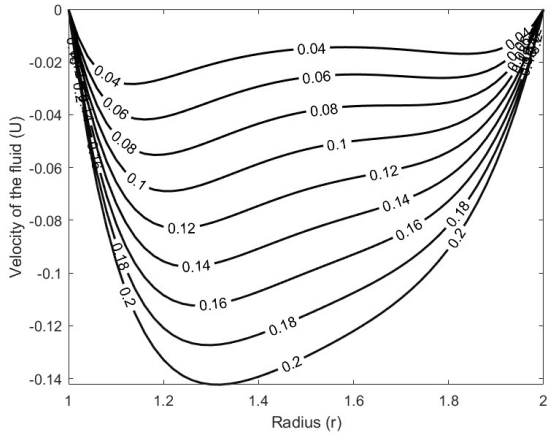

Figure 2. Velocity of the fluid for different values of time t, $(a = b = c = d = 0, \sigma_1 = \sigma_2 = 0, \lambda = 2.0, \tau = 0, \iota = 0)$.

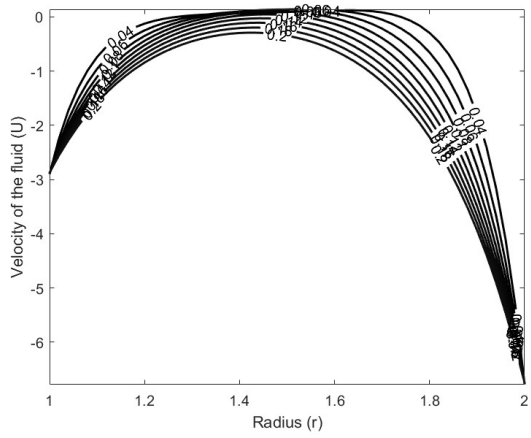

Figure 3. Velocity of the fluid for different values of time t, $(a = 0.1, b = 0.2, c = 0.3, d = 0.4, \sigma_1 = \sigma_2 = 0.5, \lambda = 2.0, \tau = 0, \iota = 0)$.

6. RESULTS AND DISCUSSION

In this section, findings from the computations using graphs obtained from Matlab are analysed extensively for the velocity profile of the fluid and dust particles, skin frictions at $r = 1$ and $r = \lambda$ for the fluid and dust particles as well as the Dean vorticities for the fluid and dust particles respectively.

6.1. VELOCITY PROFILE

In Fig. 2, the velocity profiles demonstrate a parabolic shape, symmetric about the radial midpoint. As time progresses, the velocity increases uniformly, beginning from zero, with no oscillatory effects or boundary contributions. This behaviour is primarily due to diffusion-driven momentum transfer within the fluid. In contrast, when oscillatory boundary conditions are introduced, the velocity profiles in Fig. 3 exhibit wave-like behaviour, breaking the symmetry observed in Fig. 2. These oscillatory effects propagate through the fluid domain, indicating a dynamic interplay between diffusion and boundary-induced oscillations. The combination of oscillatory parameters and boundary values adds complexity to the velocity field.

When non-zero boundary constants are applied, the velocity

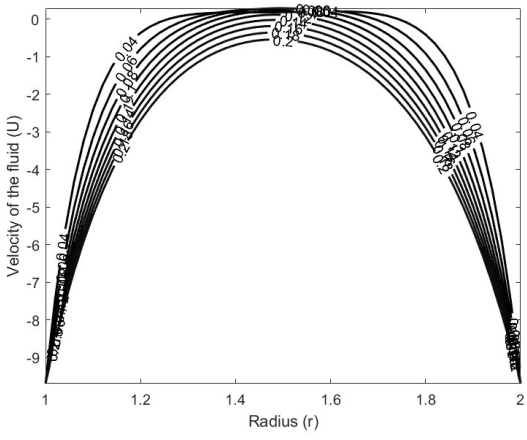

Figure 4. Velocity of the fluid for different values of time t, ($a = b = c = d = 0.5, \sigma_1 = \sigma_2 = 0.0, \lambda = 2.0, \tau = 0, \iota = 0$).

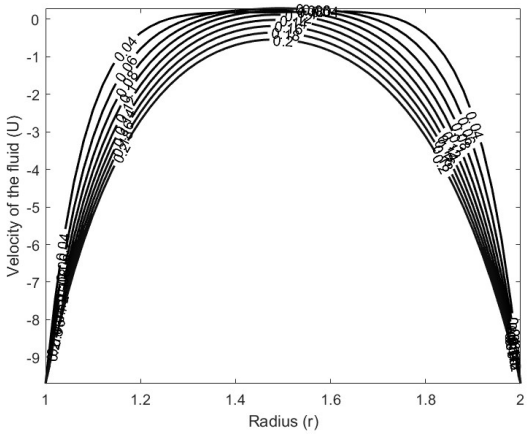

Figure 5. Velocity of the fluid for different values of time t, ($a = b = c = d = 0.5, \sigma_1 = \sigma_2 = 0.5, \lambda = 2.0, \tau = 0, \iota = 0$).

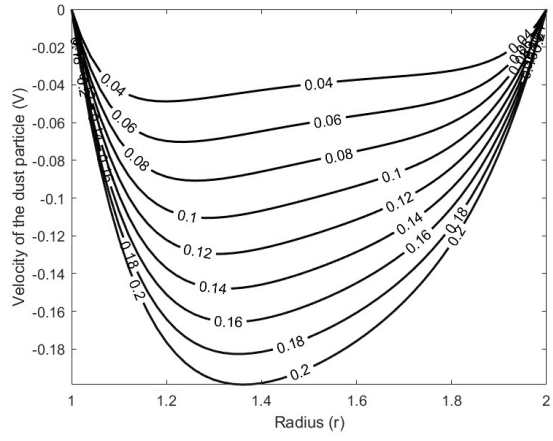

Figure 6. Velocity of the dust particles for different values of time t, ($a = b = c = d = 0.0, \sigma_1 = \sigma_2 = 0.0, \lambda = 2.0, \tau = 1.0, \iota = 1.0$).

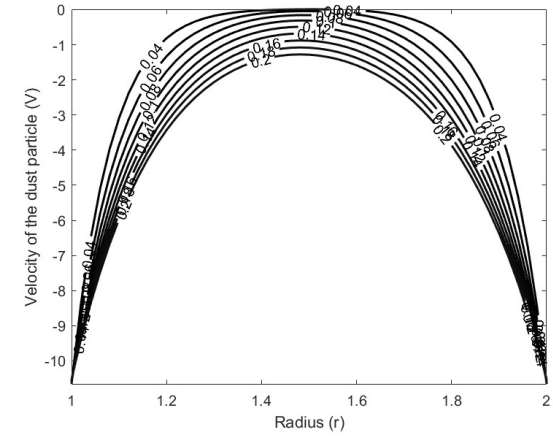

Figure 7. Velocity of the dust particles for different values of time t, ($a = b = c = d = 0.5, \sigma_1 = \sigma_2 = 0.5, \lambda = 2.0, \tau = 1.0, \iota = 1.0$).

profiles (Fig. 4) display a more pronounced parabolic shape, with higher magnitudes compared to Figs. 2 and 3. The constant boundary values uniformly enhance the flow magnitude across the radial domain without introducing oscillations. Moreover, when oscillatory forcing is combined with these boundary constants, as shown in Fig. 5, the velocity profiles exhibit amplified oscillatory behaviour. These oscillations are more pronounced near the boundaries and gradually diminish toward the center.

Thus, the interaction between oscillatory forcing and enhanced boundary flow creates a more dynamic velocity field compared to Fig. 3 and 4. The velocity profiles of dust particles under (Fig. 6) reveal a parabolic shape similar to the fluid velocity in Fig. 2. However, the dust particles exhibit a delayed response due to the relaxation parameter τ. Over time, the dust particles gradually align with the fluid velocity, demonstrating the impact of the relaxation dynamics.

Furthermore, with oscillatory boundary forcing and non-zero boundary values, the velocity profiles of the dust particles (Fig. 7) show wave-like behaviour. While the oscillations are similar to those in Figure 5 for the fluid, they are notably smoother due to the influence of the relaxation parameter. This underscores the

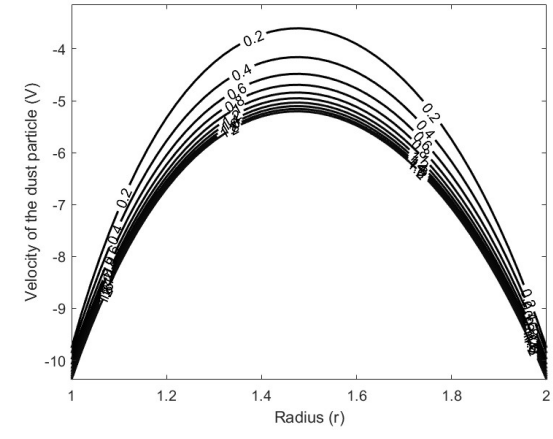

Figure 8. Velocity of the dust particles for different values of τ, ($a = b = c = d = 0.5, \sigma_1 = \sigma_2 = 0.5, \lambda = 2.0, t = 0.8, \iota = 1.0$).

moderating effect of τ on the oscillatory dynamics of the dust particles. The influence of the relaxation time τ on dust particle velocity is evident in Fig. 8. As τ increases, the dust velocity

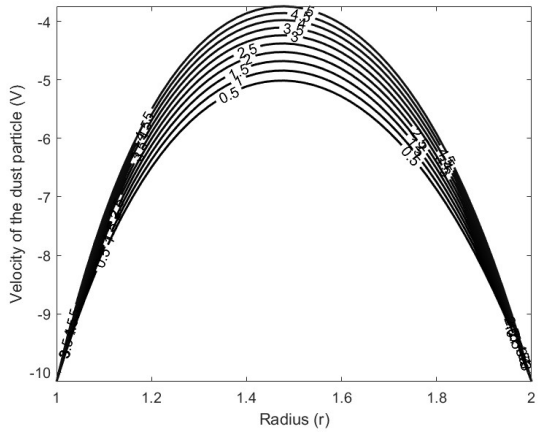

Figure 9. Velocity of the dust particles for different values of ι, ($a = b = c = d = 0.5, \sigma_1 = \sigma_2 = 0.5, \lambda = 2.0, t = 0.8, \tau = 1.0$).

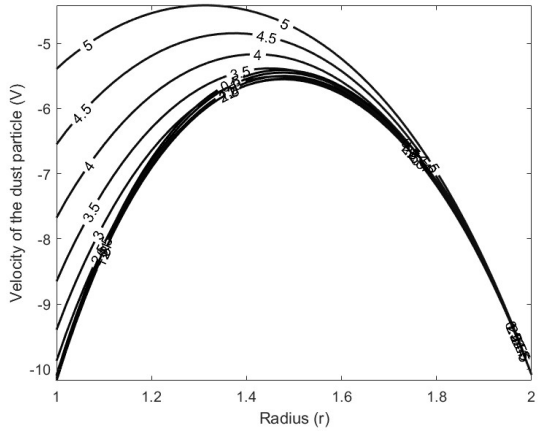

Figure 10. Velocity of the dust particles for different values of σ_1, ($a = b = c = d = 0.5, \sigma_2 = 0.5, \lambda = 2.0, t = 0.8, \tau = 1.0, \iota = 1.0$).

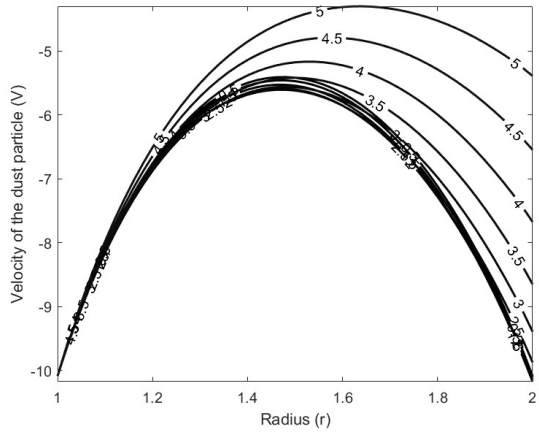

Figure 11. Velocity of the dust particles for different values of σ_2, ($a = b = c = d = 0.5, \sigma_1 = 0.5, \lambda = 2.0, t = 0.8, \tau = 1.0, \iota = 1.0$).

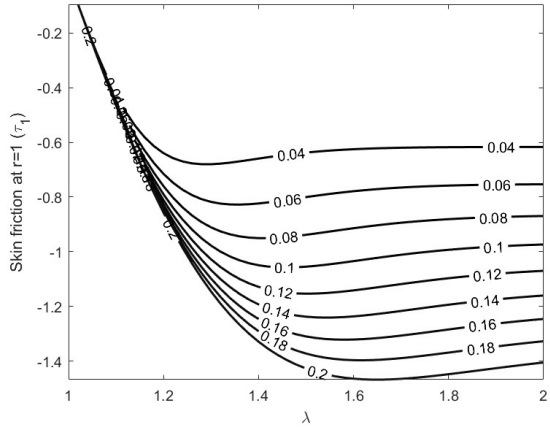

Figure 12. Skin friction of the fluid at $r = 1$, ($a = b = c = d = 0, \sigma_1 = \sigma_2 = 0, \tau = 0, \iota = 0$).

becomes increasingly delayed in aligning with the fluid velocity. This indicates that larger τ values result in greater resistance to instantaneous changes, thereby slowing the response of the dust particles to fluid motion.

The effect of mass concentration ι is illustrated in Fig. 9. As ι increases, the coupling between the fluid and dust particles strengthens, leading to a closer alignment of dust velocity with fluid velocity. This demonstrates the critical role of ι in determining the degree of interaction between the two phases. The parameter σ_1 governs oscillations originating from the inner boundary. As shown in Fig. 10, increasing σ_1 intensifies oscillatory behaviour near the inner boundary, though the effects diminish toward the center. Similarly, σ_2 controls oscillations at the outer boundary. Fig. 11 demonstrates that increasing σ_2 enhances oscillations near the outer edge, with limited propagation toward the center. Together, σ_1 and σ_2 dictate the overall oscillatory dynamics within the fluid-dust system.

SKIN FRICTIONS

Skin friction of the fluid at $r = 1$

In Fig. 12, the skin friction of the fluid at $r = 1$ exhibits an initial increase with time before stabilizing. This behavior is consistent with the momentum diffusion process, where the absence of oscillatory boundary forcing and coupling terms results in a purely diffusion-driven dynamic.

When non-zero boundary constants are applied, as in Fig. 13, the skin friction magnitude increases significantly compared to Fig. 12. The inclusion of boundary constants enhances the flow strength near the surface, thereby increasing skin friction at the boundary.

With oscillatory boundary conditions, the skin friction profile becomes highly dynamic. Oscillatory forcing induces periodic variations in skin friction, which are superimposed on the base flow, resulting in an alternating increase and decrease in the friction magnitude. This reflects the interaction of oscillatory forcing with boundary flow dynamics.

In Fig. 15, the dust particle skin friction at $r = 1$ increases gradually with time. The relaxation parameter τ governs the delay in alignment of dust velocity with the fluid, resulting in a smoother time evolution of skin friction compared to the fluid.

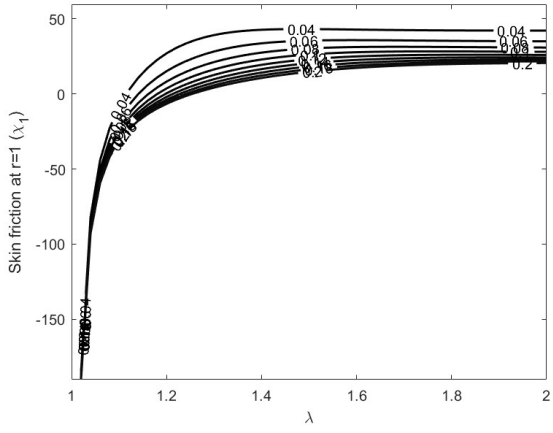

Figure 13. Skin friction of the fluid at $r = 1$, ($a = 0.1, b = 0.2, c = 0.3, d = 0.4, \sigma_1 = \sigma_2 = 0, \tau = 0, \iota = 0$).

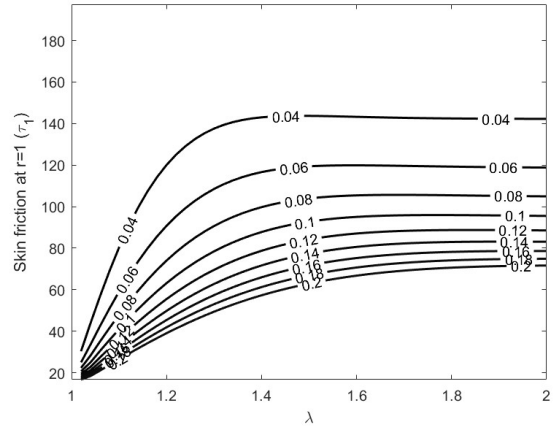

Figure 14. Skin friction of the fluid at $r = 1$, ($a = b = c = d = 0.5, \sigma_1 = \sigma_2 = 0.5, \tau = 0, \iota = 0$).

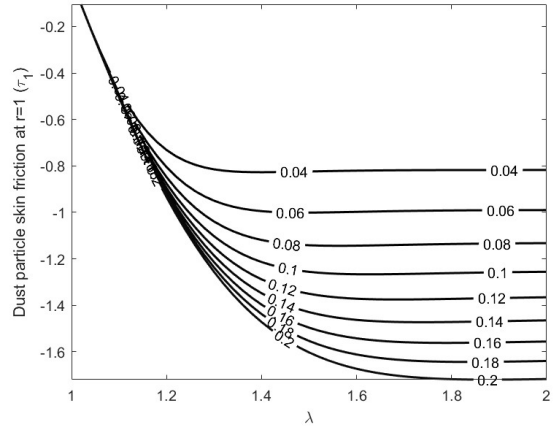

Figure 15. Dust particle skin friction of the fluid at $r = 1$, ($a = b = c = d = 0, \sigma_1 = \sigma_2 = 0, \tau = 1, \iota = 1$).

In contrast, with oscillatory boundary forcing ($\sigma_1 = \sigma_2 = 0.5$) and non-zero boundary constants, as shown in Fig. 16, the skin friction exhibits oscillations. The coupling between dust and

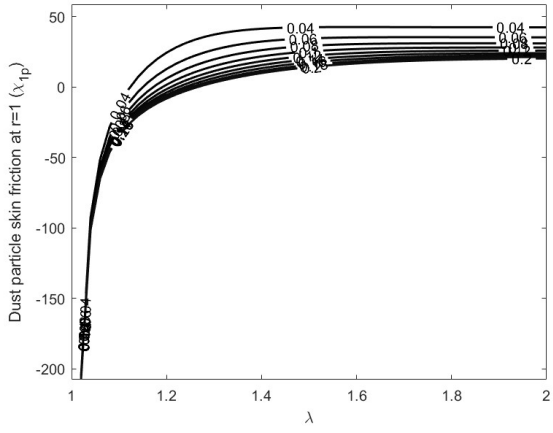

Figure 16. Dust particle skin friction of the fluid at $r = 1$, ($a = 0.1, b = 0.2, c = 0.3, d = 0.4, \sigma_1 = \sigma_2 = 0.5, \tau = 1.0, \iota = 1.0$).

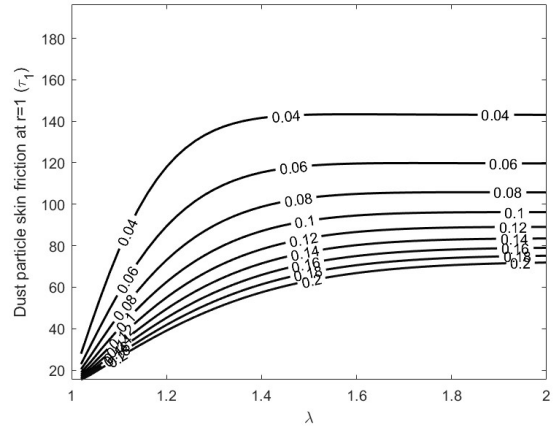

Figure 17. Dust particle skin friction of the fluid at $r = 1$, ($a = b = c = d = 0.5, \sigma_1 = \sigma_2 = 0.5, \tau = 1.0, \iota = 1.0$).

fluid amplifies the effect of boundary oscillations, leading to periodic variations in skin friction. The dust particle skin friction profile of Fig. 17 shows a more pronounced oscillatory pattern. The combination of enhanced boundary flow and oscillatory forcing intensifies the periodic nature of the skin friction dynamics. The peaks and troughs are sharper compared to Figs. 15 and 16, indicating a stronger response to boundary conditions.

The impact of the relaxation parameter τ on dust particle skin friction is evident in Fig. 18. As τ increases, the friction magnitude decreases, and the response becomes delayed. This indicates that larger τ values reduce the rate of alignment between dust and fluid velocities, thereby weakening the skin friction at the boundary.

Fig. 19 highlights the influence of ι on dust particle skin friction. Higher values of ι strengthen the coupling between fluid and dust, resulting in an increase in skin friction magnitude. The stronger coupling leads to a more rapid alignment of dust velocity with the fluid, thereby increasing the boundary friction. As σ_1 increases, the oscillatory behaviour of dust particle skin friction intensifies near the boundary (Fig. 20). The peaks and troughs become more pronounced, reflecting the greater influence of os-

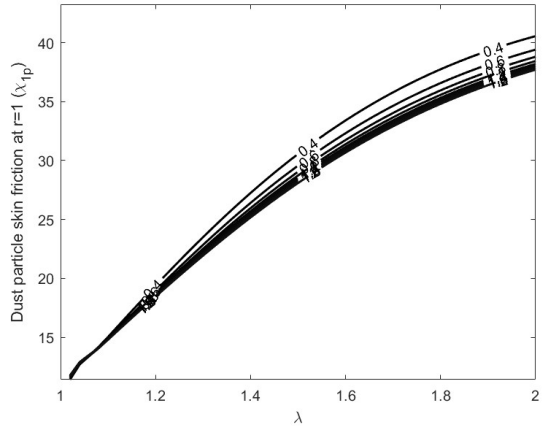

Figure 18. Dust particle skin friction of the fluid at $r = 1$ for different values of τ, ($a = b = c = d = 0.5, \sigma_1 = \sigma_2 = 0.5, t = 0.8, \iota = 1.0$).

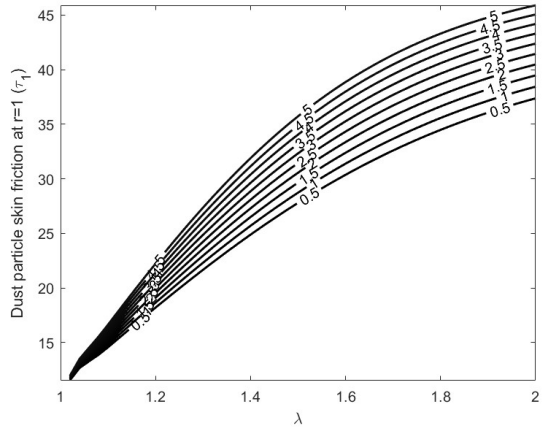

Figure 19. Dust particle skin friction of the fluid at $r = 1$ for different values of ι, ($a = b = c = d = 0.5, \sigma_1 = \sigma_2 = 0.5, t = 0.8, \tau = 1.0$).

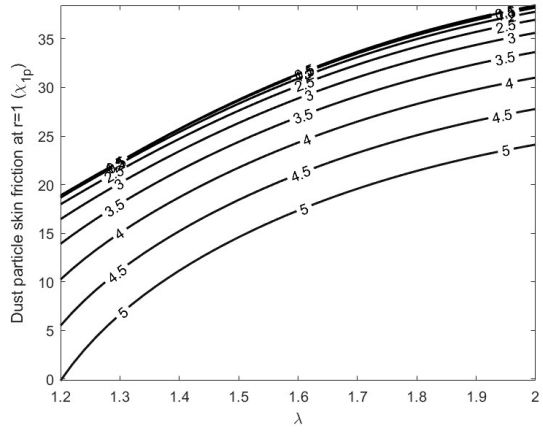

Figure 20. Dust particle skin friction of the fluid at $r = 1$ for different values of σ_1, ($a = b = c = d = 0.5, \sigma_2 = 0.5, t = 0.8, \tau = 1.0, \iota = 1.0$).

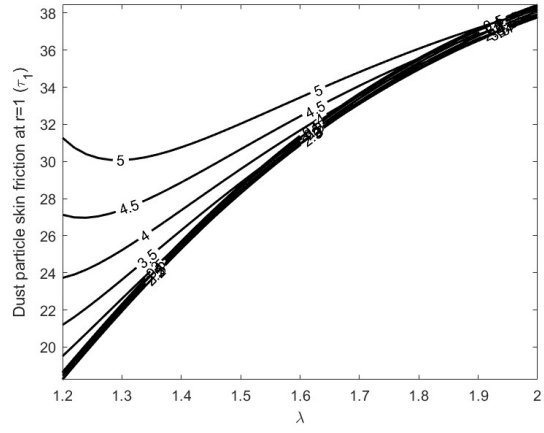

Figure 21. Dust particle skin friction of the fluid at $r = 1$ for different values of σ_2, ($a = b = c = d = 0.5, \sigma_1 = 0.5, t = 0.8, \tau = 1.0, \iota = 1.0$).

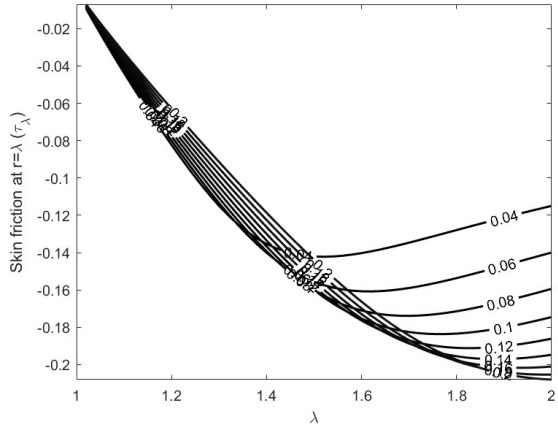

Figure 22. Skin friction of the fluid at $r = \lambda$, ($a = b = c = d = 0, \sigma_1 = \sigma_2 = 0, \tau = 0, \iota = 0$).

cillatory forcing from the inner boundary.

Similarly, increasing σ_2 (Figure 21) enhances the oscillatory nature of the skin friction at $r = 1$, but the effect originates from the outer boundary. Together, σ_1 and σ_2 determine the overall oscillatory dynamics of the system, with σ_1 dominating the inner boundary and σ_2 the outer boundary.

Skin friction at $r = \lambda$

Graphical analysis for the skin frictions at $r = \lambda$ are given below for the various governing dimensionless parameters.

In Fig. 22, the skin friction at $r = \lambda$ exhibits a gradual increase with time before stabilizing. The absence of oscillatory forcing and coupling terms results in a behavior driven purely by radial diffusion. The increase in skin friction reflects the build-up of momentum near the boundary over time. When non-zero boundary constants are introduced, as shown in Fig. 23, the skin friction magnitude increases significantly compared to Fig. 22. The boundary constants enhance the overall flow strength at $r = \lambda$, leading to a more pronounced increase in skin friction over time.

The inclusion of oscillatory boundary conditions in Fig. 24 results in highly dynamic skin friction profiles. The oscillatory forcing introduces periodic variations in skin friction that are superimposed on the increasing trend over time. These oscillations

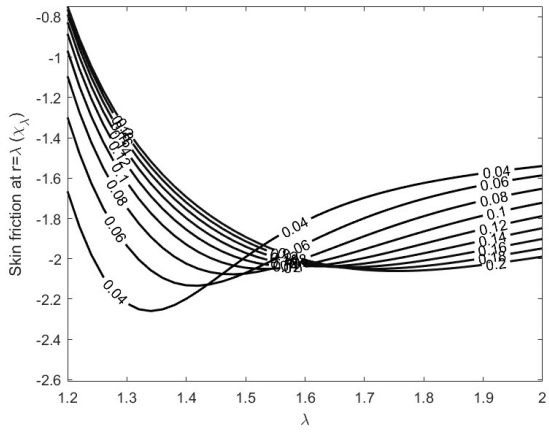

Figure 23. Skin friction of the fluid at $r = \lambda$, ($a = 0.1, b = 0.2, c = 0.3, d = 0.4, \sigma_1 = \sigma_2 = 0, \tau = 0, \iota = 0$).

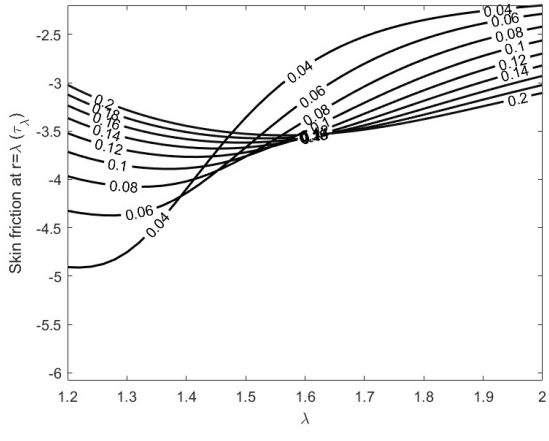

Figure 24. Skin friction of the fluid at $r = \lambda$, ($a = b = c = d = 0.5, \sigma_1 = \sigma_2 = 0.5, \tau = 0, \iota = 0$).

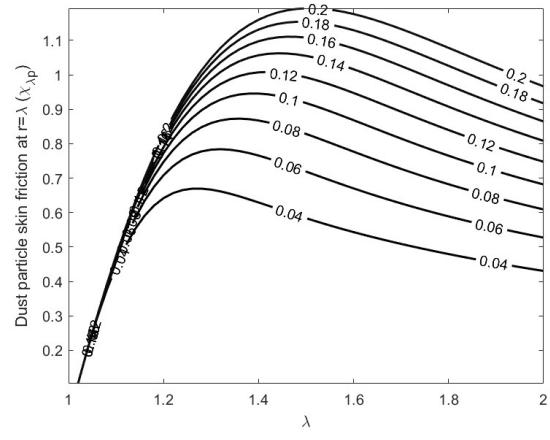

Figure 25. Dust particle skin friction of the fluid at $r = \lambda$, ($a = b = c = d = 0, \sigma_1 = \sigma_2 = 0, \tau = 1.0, \iota = 1.0$).

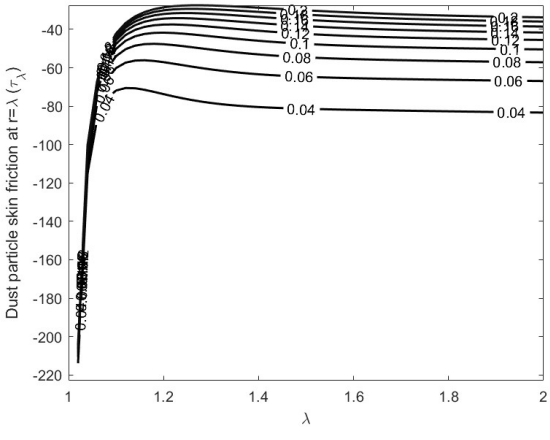

Figure 26. Dust particle skin friction of the fluid at $r = \lambda$, ($a = 0.1, b = 0.2, c = 0.3, d = 0.4, \sigma_1 = \sigma_2 = 0.5, \tau = 1.0, \iota = 1.0$).

are a direct result of the boundary-induced wave-like dynamics propagating towards $r = \lambda$.

For Fig. 25, the dust particle skin friction at $r = \lambda$ increases gradually with time. The relaxation parameter τ moderates the response of dust particles, resulting in a smoother evolution compared to the fluid. The increase in skin friction reflects the alignment of dust velocity with the fluid over time. When oscillatory forcing and non-zero boundary constants are applied, as shown in Fig. 26, the dust particle skin friction shows periodic oscillations superimposed on the increasing trend. These oscillations are smoother than those observed in Fig. 24 due to the moderating effect of the relaxation parameter.

With $a = b = c = d = 0.5$ and $\sigma_1 = \sigma_2 = 0.5$, the skin friction of dust particles at $r = \lambda$ (Fig. 27) exhibits pronounced oscillatory behavior. The combination of enhanced boundary flow and oscillatory forcing creates sharper oscillations compared to Figs. 25 and 26. This highlights the interplay between boundary effects and coupling dynamics in shaping the skin friction.

The influence of τ on dust particle skin friction is shown in Fig. 28. As τ increases, the friction magnitude decreases, and the response becomes more delayed. Larger τ values reduce the

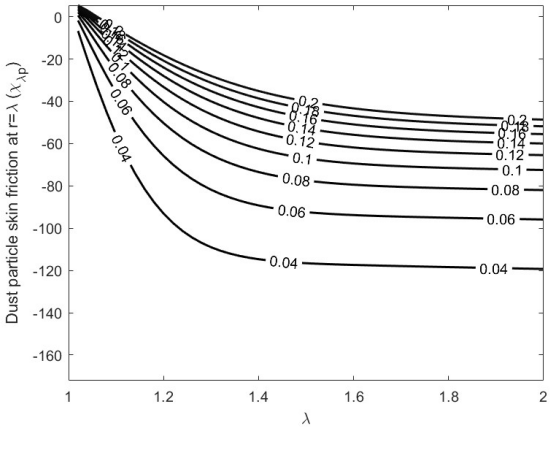

Figure 27. Dust particle skin friction of the fluid at $r = \lambda$, ($a = b = c = d = 0.5, \sigma_1 = \sigma_2 = 0.5, \tau = 1.0, \iota = 1.0$).

alignment between dust and fluid velocities, thereby weakening the skin friction at $r = \lambda$.

Fig. 29 illustrates the effect of ι on skin friction. As ι in-

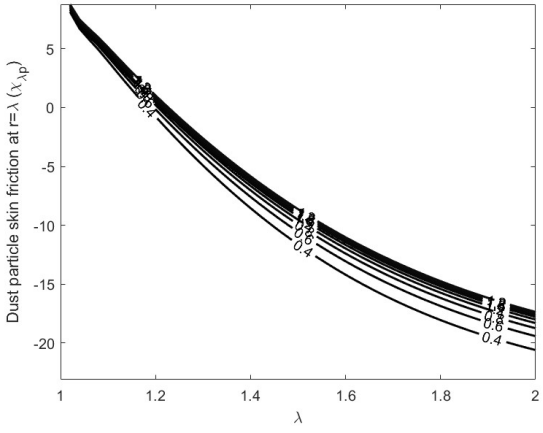

Figure 28. Dust particle skin friction of the fluid at $r = \lambda$ for different values of τ, ($a = b = c = d = 0.5, \sigma_1 = \sigma_2 = 0.5, t = 0.8, \iota = 1.0$).

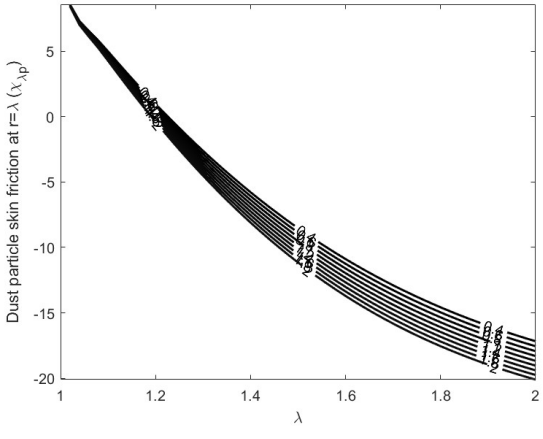

Figure 29. Dust particle skin friction of the fluid at $r = \lambda$ for different values of ι, ($a = b = c = d = 0.5, \sigma_1 = \sigma_2 = 0.5, t = 0.8, \tau = 1.0$).

creases, the coupling between fluid and dust becomes stronger, resulting in higher skin friction at $r = \lambda$. This indicates that mass concentration plays a significant role in enhancing the interaction between the two phases. Increasing σ_1 leads to more pronounced oscillations in skin friction near $r = \lambda$, as shown in Fig. 30. The peaks and troughs become sharper, reflecting the influence of oscillatory forcing from the inner boundary.

Similarly, increasing σ_2 amplifies the oscillatory behavior at $r = \lambda$, as seen in Fig. 31. The oscillations originate from the outer boundary, complementing the effects observed for σ_1. Together, these parameters govern the oscillatory dynamics of the system, with distinct contributions from each boundary.

6.2. VORTICITY

Dean vorticity is the rotational velocity within the fluid. The followings are graphical representation of the Dean vorticity for the various dimensionless parameters governing the flow.

Fig. 32 illustrates the vorticity of the fluid for different values of time t. The vorticity profiles are symmetric and increase with time, depicting a steady build-up of rotational fluid dynamics around $r = 2.0$. The absence of coupling and oscillatory terms

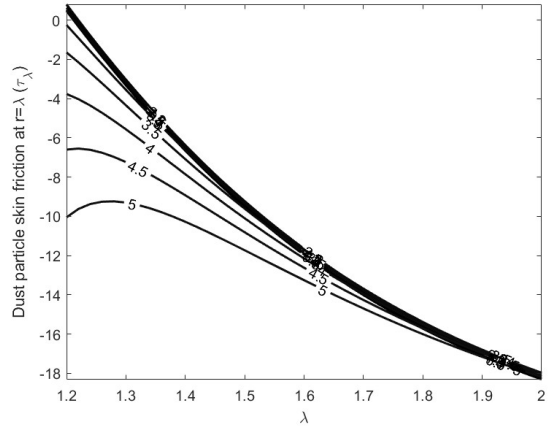

Figure 30. Dust particle skin friction of the fluid at $r = \lambda$ for different values of σ_1, ($a = b = c = d = 0.5, \sigma_2 = 0.5, t = 0.8, \tau = 1.0, \iota = 1.0$).

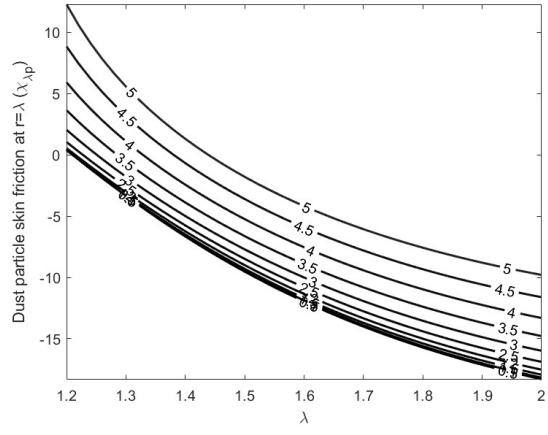

Figure 31. Dust particle skin friction of the fluid at $r = \lambda$ for different values of σ_2, ($a = b = c = d = 0.5, \sigma_1 = 0.5, t = 0.8, \tau = 1.0, \iota = 1.0$).

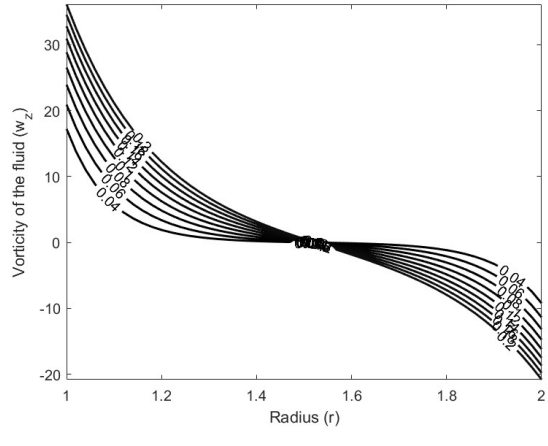

Figure 32. Vorticity of the fluid ($a = b = c = d = 0, \sigma_1 = \sigma_2 = 0, \lambda = 2.0, \tau = 0, \iota = 0$).

results in a pure diffusion-dominated vorticity pattern, indicating a direct dependence of vorticity magnitude on radial position and time. For dust particles, Fig. 33 under similar conditions but with

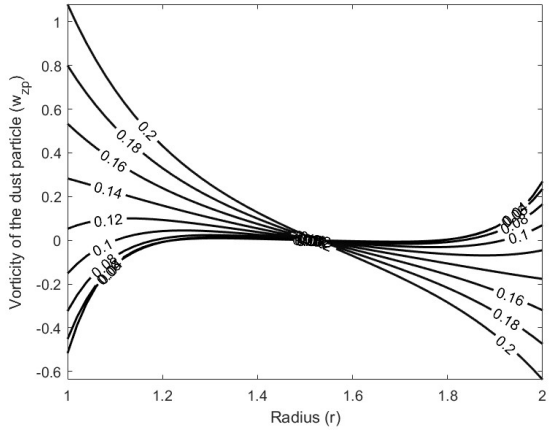

Figure 33. Vorticity of the dust particles $(a = b = c = d = 0.0, \sigma_1 = \sigma_2 = 0.0, \lambda = 2.0, \tau = 0.5, \iota = 1.0)$**.**

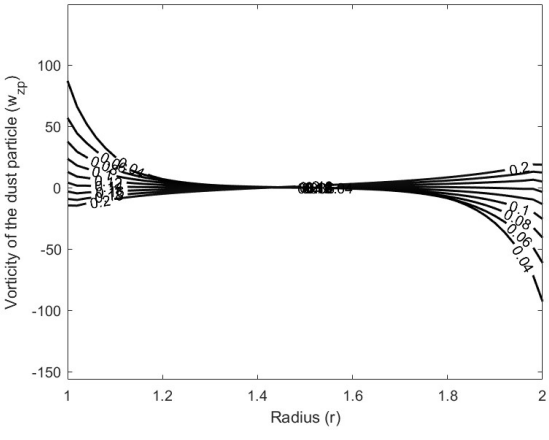

Figure 34. Vorticity of the dust particles $(a = b = c = d = 0.5, \sigma_1 = \sigma_2 = 0.5, \lambda = 2.0, \tau = 0.5, \iota = 1.0)$**.**

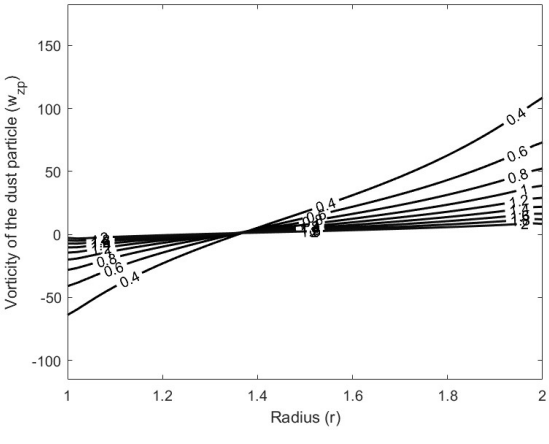

Figure 35. Vorticity of the dust particles for different values of τ**,** $(a = b = c = d = 0.5, \sigma_1 = \sigma_2 = 0.5, \lambda = 2.0, t = 0.8, \iota = 1.0)$**.**

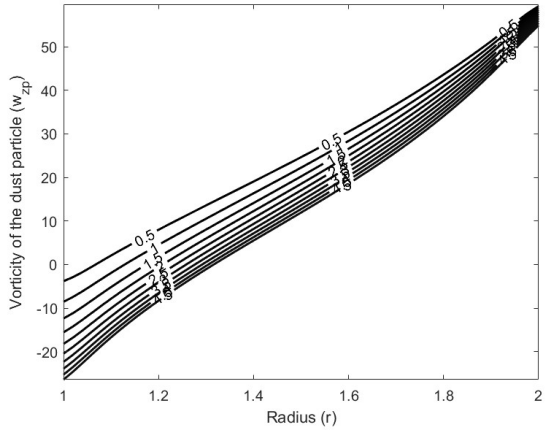

Figure 36. Vorticity of the dust particles for different values of ι**,** $(a = b = c = d = 0.5, \sigma_1 = \sigma_2 = 0.5, \lambda = 2.0, t = 2.0, \tau = 1.0)$**.**

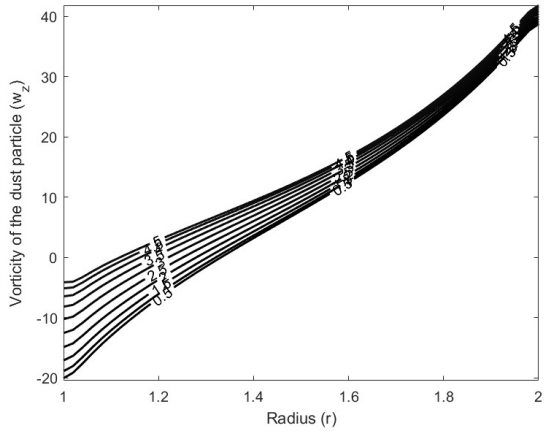

Figure 37. Vorticity of the dust particles for different values of σ_1**,** $(a = b = c = d = 0.5, \sigma_2 = 0.5, \lambda = 2.0, t = 0.8, \tau = 1.0, \iota = 1.0)$**.**

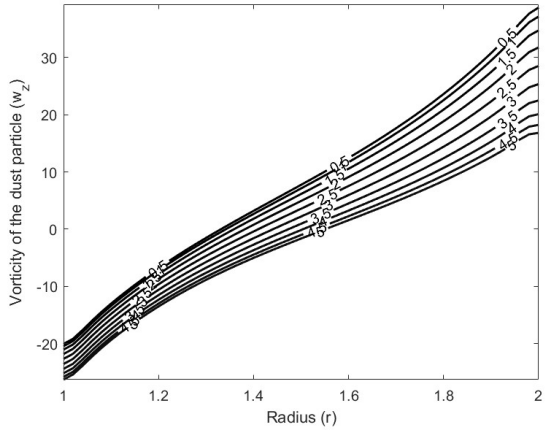

Figure 38. Vorticity of the dust particles for different values of σ_2**,** $(a = b = c = d = 0.5, \sigma_1 = 0.5, \lambda = 2.0, t = 0.8, \tau = 1.0, \iota = 1.0)$**.**

$\tau = 0.5$, $\iota = 1.0$, the vorticity shows a gradual increase but with a more moderated profile compared to the fluid. This is indicative of the relaxation and coupling effects, where τ and ι soften the intensity and rate of change of vorticity due to the interaction between the dust particles and the fluid. With Fig. 34, the vorticity for dust particles shows dramatic oscillations superim-

posed on the increasing trend, reflecting the combined effect of oscillatory forcing and boundary values. This interaction results in more complex, dynamically varying vorticity profiles that signify strong boundary and initial condition influences.

Vorticity's response to different values of τ of Fig. 35 demonstrates a clear dependency on the relaxation time. Higher τ values result in more subdued vorticity oscillations, suggesting that increased relaxation times dampen the dynamic response of dust particles to the fluid's motion.

Changes in mass concentration (ι) as demonstrated in Fig. 36 also significantly affect the vorticity of dust particles. An increase in ι results in higher vorticity magnitudes, showing that stronger coupling between fluid and particles amplifies the rotational dynamics at the given radial position.

The variation of σ_1 as depicted in Fig. 37 shows a pronounced effect on vorticity, with increased values leading to more intense and higher-frequency oscillations. This indicates the strong impact of inner boundary – driven oscillatory inputs on the vorticity profiles of dust particles. Similarly, in Fig. 38, changing σ_2 adjusts the vorticity profiles, particularly influencing how these oscillations manifest near the outer boundary. An increase in $\sigma_1 2$ intensifies the oscillatory behavior, highlighting its role in dictating the outer boundary conditions' influence on dust particle dynamics. Overall, the vorticity profiles reveal that secondary flow structures, specifically Dean vortices, emerge as a direct response to the curved geometry of the cylinders. These structures result from the relationship between centrifugal forces and the azimuthal pressure gradient, contributing to the complex rotational behaviour of the flow within the annular region.

7. CONCLUSIONS

Unsteady-state Dean flow formation of a non-Newtonian fluid in an annulus where the boundary oscillates with an angular velocity of σ_1 and σ_2 respectively. The physical mathematical models governed by momentum and continuity equations are non-dimensionlized using dimensionless parameters. The dimensionless equations are solved using two-step approach based on Laplace transformation and RSA of Laplace inversion. Velocity of the fluid, dust particles velocity, skin frictions at $r = 1$ and $r = \lambda$, and Dean vorticities of the fluid and dust particles are obtained in Laplace domain and for validations, the corresponding steady-state solutions are obtained in closed form. The most significant results are summarized as follows. They are itemized as thus:

1 Under non-oscillatory boundary conditions, the fluid velocity is primarily governed by diffusion processes, showing a smooth, parabolic increase in velocity profiles across the radial domain.

2 Introduction of oscillatory boundary conditions results in dynamic, wave-like velocity profiles, indicating a strong dependence of fluid dynamics on boundary-driven oscillatory inputs.

3 The relaxation time significantly decreases the velocity response of dust particles, leading to a delayed alignment with the fluid velocity.

4 Increased mass concentration enhances the velocity of the dust particles.

5 Skin friction at $r = 1$ increases with non-zero boundary constants, reflecting the direct impact of boundary strength on near-wall fluid behavior.

6 Oscillatory boundary conditions introduce periodic fluctuations in skin friction, underlining the influence of boundary conditions on near-wall turbulence characteristics.

7 Skin friction at $r = \lambda$ shows a time-dependent increase, with a stabilized profile over longer periods, indicating a steady state reached by the system under constant conditions.

8 The impact of τ and ι on skin friction at this radial position reveals how these parameters dampen or amplify the frictional forces at the boundary, affecting the overall system stability.

9 Vorticity in the fluid exhibits a symmetrical build-up centered around the middle of the radial domain, driven primarily by diffusion processes.

10 The magnitude of vorticity increases over time, indicating a progressive intensification of rotational fluid dynamics.

11 Oscillatory boundary conditions significantly affect the vorticity of dust particles, introducing complex, high-frequency oscillations that reflect the dynamic interaction between the particles and the fluid's oscillatory nature.

12 Higher values of τ tend to suppress these oscillations, showing the relaxation parameter's critical role in moderating the dust particles' rotational response.

LIMITATION OF THE STUDY AND FUTURE WORK

This study has certain limitations, including the assumption of uniform particle size and the neglect of fluid compressibility, which may affect accuracy in real-world applications. Future work should address these factors by incorporating variable particle sizes, compressible fluid effects, and extending the model to three-dimensional geometries. Experimental validation is also recommended to confirm the model's practical reliability.

DATA AVAILABILITY

The data will be available on request from the corresponding author.

References

[1] P. G. Saffman, "On the stability of laminar flow of a dusty gas", Journal of Fluid Mechanics **13** (1962) 120. https://doi.org/10.1017/S0022112062000555.

[2] D. H. Micheal & P. W. Norey, "The laminar flow of a dusty gas between two rotating cylinders", The Quarterly Journal of Mechanics & Applied Mathematics **21** (1968) 375. https://doi.org/10.1093/qjmam/21.3.375.

[3] D. A. Miller, "Dusty fluid round a cylinder in oscillatory rotation", Applied Scientific Research **20** (1969) 81. https://doi.org/10.1007/BF00382385.

[4] Y. B. Reddy, "Flow of a dusty gas through elliptical annulus", Japanese Journal of Applied Physics **12** (1973) 16. https://iopscience.iop.org/article/10.1143/JJAP.12.1628.

[5] R. K. Gupta & S. C. Gupta, "Unsteady flow of a dusty gas in cylinders with circular and sectorial cross sections", Proceedings of Indian Academy of Science. Section A **86** (1977) 591. https://doi.org/10.1007/BF03046915.

[6] P. Mitra & P. Bhattacharyya, "Unsteady hydromagnetic laminar flow of a conducting dusty fluid between two parallel plates started impulsively from rest", Acta Mech. **39** (1981) 171. https://doi.org/10.1007/BF01170340.

[7] E. Rukmangadachari & P. V. Arunachalam, "Dusty viscous flow through a cylinder of triangular cross-section", Proceedings of Indian Academy of Science - Mathematical Sciences. Part A **88** (1979) 169. https://doi.org/10.1007/BF02871614.

[8] L. Debnath & A. K. Ghosh, "On unsteady hydromagnetic flows of a dusty fluid between two oscillating plates", Applied Scientific Research **365** (1988) 353. https://doi.org/10.1007/BF00457067.

[9] M. H. Hamdan & R. M. Barron, "A dusty gas flow model in porous media", Journal of Computational and Applied Mathematics **30** (1990) 21. https://doi.org/10.1016/0377-0427(90)90003-I.

[10] K. Vajravelu & J. Nayfeh, "Hydromagnetic flow of a Dusty fluid over a stretching sheet", International Journal of Non-Linear Mechanics **27** (1992) 937. https://doi.org/10.1016/0020-7462(92)90046-A.

[11] M. H. Hamdan & R. M. Baron, "On the Darcy-Lapwood-Brinkman-Saffman dusty fluid flow models through porous media part I: models development", Appl. Math. Comput. **54** (1993) 65. https://doi.org/10.1016/0096-3003(93)90033-B.

[12] X. Yang, S. Eidelman & I. Lottati, "Shock-wave reflection over a semi-circular cylinder in a dusty gas", AIAA Journal **31** (1993) 1737. https://doi.org/10.2514/3.11842.

[13] N. Datta & D. C. Dalal, "Pulsatile flow and heat transfer of a dusty fluid through an infinitely long annular pipe", International Journal of Multiphase Flow **21** (1995) 515. https://doi.org/10.1016/0301-9322(94)00064-Q.

[14] H. A. Atria, "Influence of temperature-dependent viscosity on the MHD-channel flow of dusty fluid with heat transfer", Acta Mechanica **151** (2001) 89. https://doi.org/10.1007/BF01272527.

[15] F. M. Allan, N. Qatanani, I. Barghouthi & K. M. Takatka, "Dusty gas model of flow through naturally occurring porous media", Appl. Math. Comput. **148** (2004) 809. https://doi.org/10.1016/S0096-3003(02)00939-6.

[16] A. N. Volkov & Y. M. Tsirkunov, "Effect of a dispersed admixture on the flow pattern and heat transfer in a supersonic dusty-gas flow around a cylinder", Fluid Dynamics **40** (2005) 561. https://doi.org/10.1007/s10697-005-0095-3.

[17] B. J. Gireesha, C. S. Bagewadi & B. C. Prasannakumar, "Pulsatile flow of an unsteady dusty fluid through rectangular channel", Commun. Nonlinear Sci. Numer. Simul. **14** (2009) 2103. https://doi.org/10.1016/j.cnsns.2008.06.015.

[18] B. J. Gireesha, C. S. Bagewadi & B. C. Prasannakumar, "Flow of unsteady dusty fluid under varying pulsatile pressure gradient in anholonomic co-ordinate system", Electronic Journal Theoretical Physics **4** (2007) 9. https://openurl.ebsco.com/contentitem/gcd:24993549?sid=ebsco:plink:scholar&id=ebsco:gcd:24993549&crl=c.

[19] O. D. Makinde & T. Chinyoka, "MHD transient flows and heat transfer of dusty fluid in a channel with variable physical properties and Navier slip condition", Comput. Math. Appl. **60** (2010) 660. https://doi.org/10.1016/j.camwa.2010.05.014.

[20] P. Eguía, J. Zueco, E. Granada & D. Patiño, "NSM solution for unsteady MHD Couette flow of a dusty conducting fluid with variable viscosity and electric conductivity", Appl. Math. Model **35** (2011) 303. https://doi.org/10.1016/j.apm.2010.06.005.

[21] B. K. Jha & Y. J. Danjuma, "Transient generalized Taylor–Couette flow of a dusty fluid: A semi-analytical approach", Partial Differ. Equ. Appl. Math. **5** (2022) 100400. https://doi.org/10.1016/j.padiff.2022.100400.

[22] B. K. Jha & J. D. Yahaya, "Transient Dean flow in an annulus: a semi-analytical approach", Journal of Taibah University for Science **13** (2018) 169. https://doi.org/10.1080/16583655.2018.1549529.

[23] B. K. Jha & Y. J. Danjuma, "Impact of variable viscosity on unsteady couette flow", Heat Transfer (2025) 1–17. https://doi.org/10.1002/htj.23263

[24] B. K. Jha & Y. J. Danjuma, "Unsteady dean flow formation in an annulus with partial slippage: a Riemann-sum approximation approach", Results in Engineering **5** (2020) 100078. https://doi.org/10.1016/j.rineng.2019.100078.

[25] B. K. Jha & Y. J. Danjuma, "Transient generalized Taylor-Couette flow: a semi-analytical approach",Journal of Taibah University for Science" **14** (2020) 445. https://doi.org/10.1080/16583655.2020.1745477.

[26] Y. J. Danjuma, "Transient flow formation inside an annulus: a semi-analytical approach", 2019. [Online]. Available: https://www.morebooks.de/store/gb/book/transient-flow-formation-inside-an-annulus:-a-semi-analytical-approach/isbn/978-620-0-23920-4.

[27] B. K. Jha & Y. J. Danjuma, "Transient dean flow in a channel with suction/injection: a semi-analytical approach", Proceedings of the Institution of Mechanical Engineers, Part E: Journal of Process Mechanical Engineering **233** (2019) 1036. https://doi.org/10.1177/0954408919825718.

[28] B. K. Jha & J. O. Odengle, "Unsteady couette flow in a composite channel partially filled with porous material: a semi-analytical approach", Transport in Porous Media **107** (2015) 219. https://doi.org/10.1007/s11242-014-0434-0.

[29] D. Y. Tzou, *Macro to microscale heat transfer: the lagging behavior*, John Wiley & Sons, Ltd, 2015. https://doi.org/10.1002/9781118818275.